A Micromechanics Investigation of Sliding Wear in Coated Components

By Wenyi Yan, Esteban P. Busso and Noel P. O'Dowd

Department of Mechanical Engineering,
Imperial College,
London SW7 2BX, United Kingdom

In this work, the wear behaviour of coated components subjected to sliding contact conditions is investigated using a multiscale micromechanics approach. Periodic unit cell-type continuum mechanics models are used to predict localised deformation patterns at the scale of the coating thickness (mesoscale) and the rate of material removal due to repeated sliding contact. To that purpose, realistic contact loads determined at the component level (macroscale) are applied at the mesoscopic level. The results indicate that the deformation of the coating is controlled by the cyclic accumulation of plastic deformation, or ratchetting, at the coating subsurface. Based on a ratchetting failure criterion, a wear equation is proposed and applied to investigate parametrically the influence of the principal material, loading and surface roughness parameters on the wear rate. The results reveal that the wear rate increases with contact pressure and depends strongly on coating thickness and the roughness of the counterpart surface. It was also found that a reduction in the friction coefficient and an increase in the coating strain hardening behaviour can considerably improve the wear resistance of coated components.

Keywords: Sliding Wear, Micromechanics, Wear-resistant Coatings, Rachetting, Wear Rate

1. Introduction

Surface coatings are used extensively to improve the wear resistance of a broad variety of engineering components. It is estimated that the life of a component can be improved by up to a factor of ten if coated with an appropriate material. Traditionally, hard, brittle coatings such as TiN have been the most commonly used wear-resistant coatings. Over the last decade, however, a new generation of coating materials and processing techniques have emerged as a result of the technological growth fuelled by new industrial applications. These coatings are generally strong and ductile in nature, relatively thick (e.g. 100 to 300 μm) and exhibit beneficial self-lubricating properties, which have led to considerable improvements in their wear resistance (Monaghan *et al.*, 1993). Typical of these new coatings are Mo-based systems deposited by thermal and plasma spraying techniques, e.g. see Haferkamp *et al.* (1996) and Wayne *et al.* (1994).

To predict the wear behaviour of coating systems accurately, an understanding of the dominant wear mechanisms during service is crucial. The aim of the present study is to investigate and quantify the influence of contact loads, surface roughness and material parameters on the wear rate of a typical thick metallic coating. Wear due to sliding contact conditions is considered—abrasive and erosive wear mechanisms, such as penetration, microcutting or impinging are beyond the scope of this investigation. It is assumed that the sliding velocity is relatively slow so that any interfacial temperature rise can be considered negligible. Thermal effects and chemical interactions are therefore excluded. Furthermore, the effect of lubrication is accounted for through different values of friction coefficients between the contacting surfaces.

Sliding wear between two bodies generally involves three steps as illustrated in Fig. 1. Initially, see Fig. 1(a), localised deformation patterns develop beneath the coating surface as a result of the sliding contact loads (*e.g.*, see Dautzenberg *et al.* (1973), Ruff (1976) and Rigney *et al.* (1992)). Such localised deformation can be the precursor of micro-cracks, which form as a result of the coalescence of micro-voids nucleated at inclusions in highly deformed regions at the coating subsurface, as shown in Fig. 1(b). Continued sliding contact promotes crack growth and causes neighbouring cracks to coalesce, Fig. 1(c). Eventually, cracks propagate towards the surface at weak points and wear debris is formed.

Kapoor and Johnson (1994) have analysed the formation of debris during sliding wear tests and proposed the repeated accumulation of plastic strain, or ratchetting, as the mechanism leading to sliding wear in metals. In the proposed ratchetting wear model (Kapoor *et al.*, 1996), the material was assumed to be gradually extruded due to the cumulative plastic strain produced by the pummelling action of hard spherical particles acting normally to wedge shaped asperities. One drawback of their model is that it cannot account for the accumulation of shear deformation induced by sliding contact, which is expected to make a significant contribution to the ratchetting phenomenon.

Traditionally, low-cycle fatigue laws have been used to estimate the life of a material under sliding contact, thus treating wear essentially as a fatigue problem (e.g., see Challen *et al.*, 1986). Furthermore, fatigue based approaches have been applied to components failing under either a plastic shakedown or a ratchetting state. More recently, low cycle fatigue and ratchetting have been treated as competing failure

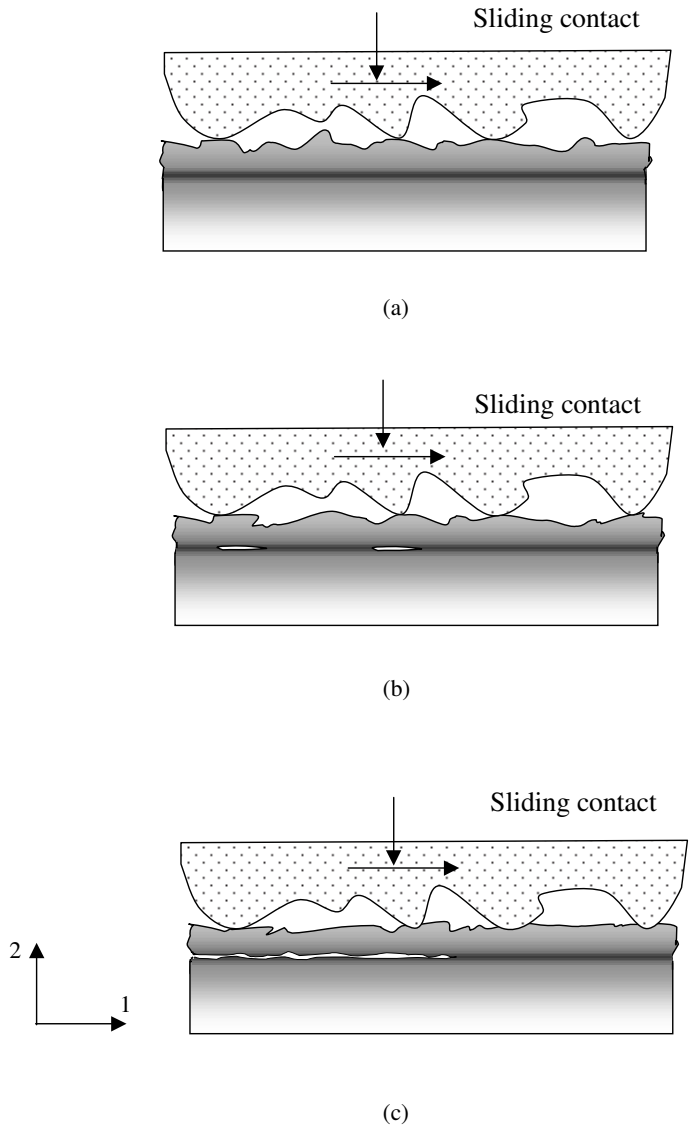

Figure 1. Schematic representation of the sliding wear process: (a) accumulated plastic deformation in the subsurface, darker regions correspond to higher levels of accumulative plastic strains; (b) subsurface crack initiation; (c) crack propagation and wear debris formation

processes with local failure considered to be controlled by the dominant mechanism. For ratchetting, the local failure of the material can be assumed to occur by a ductile mechanism linked to the exhaustion of the local ductility of the material (Kapoor, 1994). In such cases, local failure may be controlled by the accumulation of an appropriate plastic strain measure per cycle with failure occuring when

it reaches the uniaxial equivalent ductility of the material, which will in turn be controlled by the local mean triaxial stress.

In the present work, such a ratchetting-type failure law is used to quantify the wear rate of a thick metallic coating using a multiscale micromechanics approach. Compared to the size of a coated component, the coating thickness is generally very small—if a coated component is considered at the macroscale and the coating microstructure (e.g. grains) at the microscale, then the deformation at the level of the coating thickness can be treated at an intermediate or mesoscopic scale (e.g. $\sim$50 to 1000 μm). To that purpose, continuum mechanics models comprising a representative region of the coated system and the contacting body will be relied upon. The deformation behaviour of the coating will be investigated from mesoscopic unit cell studies, with contact conditions extracted from a macroscopic analysis of the industrial process of interest.

This paper is structured as follows. Details of the unit cell model and the relevant length scales are discussed in Section 2. In Section 3, the deformation patterns in the coating subsurface induced by the repeated applications of sliding contact loads are determined from the unit cell analyses. In Section 4, the ratchetting behaviour of the coating is quantified and used to motivate the formulation of a wear relation. In Section 5, the influence of several process parameters on the wear rate is investigated. Finally, discussion and conclusions are given in Sections 6 and 7, respectively.

2. Multiscale Micromechanics Approach

(a) *Unit cell model*

The stamping of a thin metal sheet using coated dies will be considered to illustrate the use of a multiscale approach in the study of sliding wear. A typical stamping process is illustrated schematically in Fig. 2(a). Here, the upper die is pushed downward towards the stationary lower die. The high contact pressures between the dies and the workpiece cause the latter to deform plastically until the required shape is obtained. A wear-resistant coating is often applied on the dies to minimize the surface wear caused by the sliding contact between the workpiece and the dies. Here, the wear rate of such coatings will be examined.

At the macroscale, when a stamping cycle reaches completion, the nominal contact area will extend over the whole die surface. However, at the mesoscale, the actual contact area is smaller than the nominal one due to the discrete nature of the contact introduced by the surface asperities of a real surface. The real contacting regions therefore cover only part of the coating surface, as illustrated in the inset to Fig. 2(a).

When two components slide relative to one another, a transient or running-in phase where initially sharp asperities are smeared out can be identified (e.g. see Suh, 1980). This is followed by a steady-state stage where the characteristics of the asperities and the wear rate remain constant. Experiments have also revealed that the steady-state wear rate is independent of the initial surface roughness (e.g., Jahanmir & Suh, 1977). Bearing in mind that a new workpiece is deformed in each stamping operation and that the dies are replaced or recoated only after a large number of stamping operations, the workpiece can therefore be considered to be

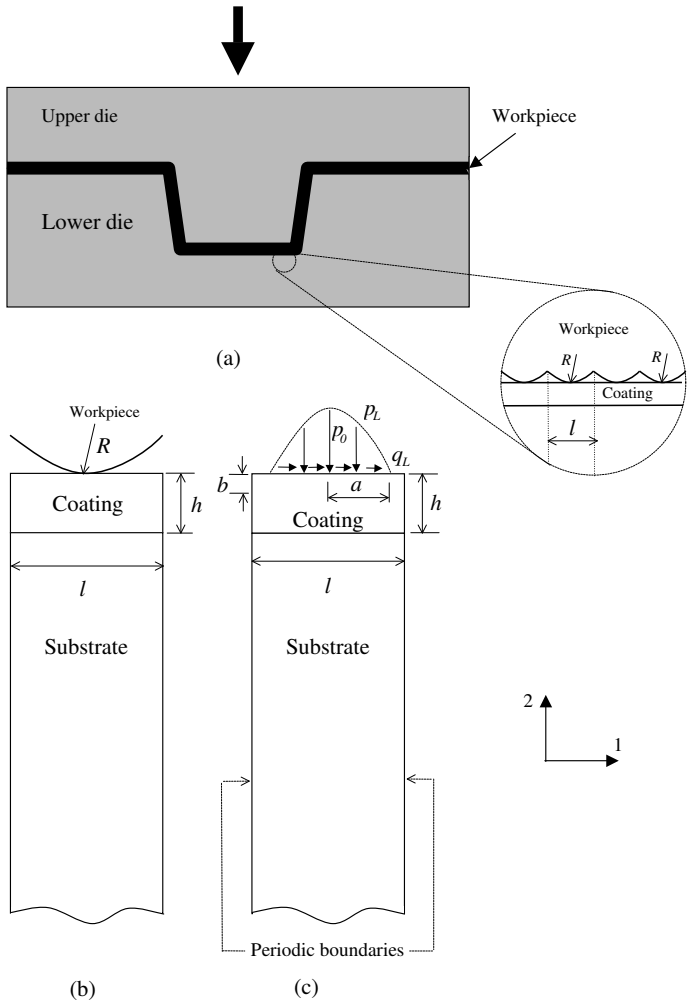

Figure 2. Illustration of the establishment of the unit cell model: (a) schematic stamping dies, (b) representative cell, (c) unit cell model

undergoing transient wear and the coating to be in the steady-state wear regime. Hence the surface coating can be assumed to be relatively smooth compared to the workpiece. In this work, the topography of the workpiece surface is idealised as periodically arranged identical asperities of contact radius, R, and the coating surface is assumed to be perfectly smooth, as illustrated in Fig. 2(a). However, note that this multiscale approach could readily be generalised to a surface containing a finite distributions of asperity radii.

During the stamping process, it is assumed that, at the mesoscale, each asperity transfers the same contact load. Thus, a representative unit cell will involve only one asperity and the neighbouring coating and substrate regions, as shown in Fig. 2(b). The influence of the adjacent material on the deformation of the unit cell

is accounted for through the use of periodic boundary conditions on the unit cell boundaries normal to the x_1 axis (see Fig. 2(c)).

The sliding contact between the asperity and the coated substructure could be simulated explicitly for a given asperity shape. However, as the focus of this study is primarily on the coating response to sliding contact and due to the large computational effort which would be involved, the workpiece asperity will not be modelled directly. Instead, its effect will be introduced through appropriately defined surface normal and shear tractions, as shown in Fig. 2(c). It should be mentioned that no variations in the contact tractions during the sliding contact cyclic history are considered as would arise in practice due to, e.g., deformation of the work piece asperity. This is however expected to introduce only small inaccuracies in the results. The use of constant normal and shear tractions defined in this way also allows a systematic study of the independent system parameters to be undertaken, as will be seen in Section 5.

The unit cell model geometry, shown in Fig. 2(c), is fully defined by the coating thickness h and the length of the unit cell, or wavelength of the periodically arranged asperities, l. The depth of the substrate is chosen to be much larger than h or l and plane strain conditions are assumed throughout.

The normal contact pressure distribution on the coating is assumed to be a Hertzian-type function. In principle, a Hertzian contact pressure applies only to elastic contact, e.g. Johnson (1985). In elasto-plastic contact problems, a Hertzian distribution is likely to overestimate the maximum contact pressure for a given contact load, as plastic deformation increases the contact area. Therefore, in this study, a modified Hertzian distribution will be used to compensate for such overestimation. For a given total contact load per unit out-of-plane width, F, acting on an asperity of initial radius R, the expressions for the maximum contact pressure, p_o, and the contact half-width, a in Fig. 2, are given by,

$$p_0 = \lambda \sqrt{\frac{1}{\pi}\frac{F\,E^*}{R}}\ , \tag{2.1}$$

$$a = \frac{1}{\lambda}\sqrt{\frac{4}{\pi}\frac{F\,R}{E^*}}\ , \tag{2.2}$$

where,

$$E^* = \left(\frac{1-\nu_c^2}{E_c} + \frac{1-\nu_a^2}{E_a}\right)^{-1} \tag{2.3}$$

and E_c, ν_c, and E_a, ν_a, are the coating and asperity material Young's modulus and Poisson's ratio, respectively. In Eq. 2.1 and 2.2, λ is a plastic modification factor. For elasto-plastic contact, $\lambda < 1$, and when $\lambda = 1$, the elastic Hertzian relations are recovered.

Normal and tangential traction distributions, indicated as $p_{_L}$ and $q_{_L}$ in Fig. 2(c), respectively, can now be fully defined in terms of p_0, the maximum Hertzian pressure and a, the contact half-width, as

$$p_{_L}(x_1) = p_0\sqrt{1-(x_1/a)^2}, \tag{2.4}$$

$$q_{_L}(x_1) = \mu\, p_{_L} = \mu p_0\sqrt{1-(x_1/a)^2}, \tag{2.5}$$

Table 1. *Substrate yield stress variations from its surface*

Distance from surface (μm)	40	150	340	500	700
Hardness (HV)	751	746	680	313	244
Yield Strength (MPa)	2500	2490	2270	1040	810

In Eq. 2.5, the Amontons-Coulomb friction law is invoked to obtain the tangential traction $q_{_L}$ in terms of the friction coefficient, μ. The subscript 'L' is used in Eq. 2.4 and 2.5 to indicate that these are 'local' (mesoscopic) stress distributions as opposed to the 'global' (macroscopic) distributions which would be determined from, e.g., a finite element analysis.

The total contact load per unit out-of-plane width, F in Eqs. 2.1 and 2.2, can be obtained from,

$$F \quad = \quad p\ l, \tag{2.6}$$

where l is the unit cell width and p the nominal contact pressure which can be determined from a finite element simulation of the actual industrial process of interest—the effect of surface roughness on p can be neglected at this (macroscale) level. The values of l and R can be estimated from the roughness characteristics of the contacting surfaces.

It should be noted that a useful relation between the nominal contact pressure acting on the unit cell and p_0 and a can be obtained from the assumed Hertzian-type contact pressure distribution given by Eq. 2.4,

$$p \quad = \quad \int_{-a}^{a} \frac{p_0}{l} \sqrt{1-(x_1/a)^2}\, dx_1 \quad = \quad \frac{\pi}{2}\ \frac{p_0\ a}{l} \quad . \tag{2.7}$$

The influence of different combinations of the independent model parameters, namely p, R, l, h, μ, and the coating hardening behaviour, on the wear rate will be discussed in Section 5.

(*b*) *Material properties and loading parameters*

The coating/substate system to be analysed consists of a Mo coating applied on a carburised steel substrate. The substrate Young's modulus and Poisson's ratio were taken as 194 GPa and 0.3, respectively. The measured hardness and corresponding yield stress data at different depth from the substrate surface are given in Table 1. These yield stress values are used in the finite element calculations.

The coating elastic modulus and Poisson's ratio were found to be 310 GPa and 0.3, respectively (COMPWERC, 1998). The coating yield stress was extracted from force-displacement curves obtained from microindentation tests on coated specimens (COMPWERC, 1998) using the method recently proposed by Tunvisut *et al.* (1999). A mean value of the yield stress for the Mo coating was found to be $\sigma_{yc} =$ 2300 MPa. This value is consistent with published data for a Mo coating (Habig, 1989). Such high strength can be related to the ~ 0.5 μm mean grain size measured in the Mo coating. Note that, following the convention used in contact mechanics, stress quantities will be normalised by the shear strength, k_c, rather than the yield stress. Here, $k_c = \sigma_{yc}/\sqrt{3} = 1300$ MPa.

The coating is assumed to be a rate independent, Von Mises material and its cyclic behaviour is described by a standard nonlinear kinematic hardening law. The coating constitutive relations are next outlined within the context of large strain kinematics.

The Jaummann rate of the Kirchhoff stress tensor, $\mathbf{T}^*$, is given as,

$$\overset{\triangledown}{\mathbf{T}}{}^* = \mathcal{L}\,[\mathbf{D} - \mathbf{D}^p] \quad , \tag{2.8}$$

where $\mathbf{D}$ is the total deformation rate tensor, $\mathbf{D}^p$ the plastic deformation rate tensor, and $\mathcal{L}$ the fourth order isotropic elasticity tensor.

The yield function is defined as,

$$\Phi = \tilde{\sigma} - \sigma_{yc} \leq 0, \tag{2.9}$$

with

$$\tilde{\sigma} = \sqrt{\frac{3}{2}\,(\mathbf{T}^{*'} - \boldsymbol{\alpha}') : (\mathbf{T}^{*'} - \boldsymbol{\alpha}')}\,, \tag{2.10}$$

where $\mathbf{T}^{*'}$ and $\boldsymbol{\alpha}'$ are the deviatoric components of $\mathbf{T}^*$ and of the kinematic tensorial hardening variable, $\boldsymbol{\alpha}$, respectively. The constitutive equation for $\mathbf{D}^p$ is given by,

$$\mathbf{D}^p = \frac{3}{2} < \dot{\bar{\epsilon}}^p > \frac{\mathbf{T}^{*'} - \boldsymbol{\alpha}'}{\tilde{\sigma}}\,, \tag{2.11}$$

where $< \dot{\bar{\epsilon}}^p >$ is a switching parameter defined as,

$$< \dot{\bar{\epsilon}}^p > = \begin{cases} \dot{\bar{\epsilon}}^p & \text{if } \Phi = 0 \quad \text{and} \quad \partial\Phi/\partial\mathbf{T}^* \,.\, \mathcal{L}[\mathbf{D}] > 0, \\ 0 & \text{otherwise,} \end{cases} \tag{2.12}$$

and $\dot{\bar{\epsilon}}^p$ represents the magnitude of the equivalent plastic strain rate. The evolution of $\boldsymbol{\alpha}$ follows a hardening-dynamic recovery form (Ziegler, 1959),

$$\dot{\boldsymbol{\alpha}} = H_c\,(\mathbf{T}^* - \boldsymbol{\alpha})\,\dot{\bar{\epsilon}}^p - C\,\boldsymbol{\alpha}\,\dot{\bar{\epsilon}}^p, \tag{2.13}$$

where, H_c and C, are dimensionless material constants which are calibrated from cyclic stress-strain data. From the uniaxial hardening behaviour of bulk Mo, it was found that $H_c = 3.04$ and $C = 3.6$. The Cauchy or true stress tensor $\mathbf{T}$ can be expressed in terms of $\mathbf{T}^*$ and the deformation gradient, $\bar{\mathbf{F}}$, as $\mathbf{T} = (\det\bar{\mathbf{F}})^{-1}\,\mathbf{T}^*$.

A macroscopic simulation of the stamping process was carried out to obtain the distribution of contact pressures along the die surfaces during a stamping operation by Tunvisut *et al.* (2000). The following values were obtained from the macroscopic FE results and the geometrical and surface characteristics of the Mo coating and workpiece,

$$h = 0.20 \text{ mm}, \quad R = 0.86 \text{ mm}, \quad \mu = 0.1\,, \tag{2.14}$$

$$l = 0.48 \text{ mm}, \quad p = 2.36 \text{ GPa}\,. \tag{2.15}$$

In normalised form, $h/l = 0.42$, $p/k_c = 1.77$, and $R/l = 1.79$. The value of p is a representative magnitude taken from regions where sliding was predicted to occur

in the FE analysis. Using a typical value for $\lambda = 0.8$ (Yan & Fischer, 1999), Eqs. 2.1 and 2.2 give $p_0 = 4.52\, k_c$ and $a = 0.25\, l$

Having established the material properties, boundary and loading conditions for the unit cell model, the mechanical response of the coating under repeated stamping operations at the mesoscale can be obtained using finite element techniques. In this work, plane strain finite element calculations of a stamping operation are carried out using the code ABAQUS (1998). The contact tractions described by Eqs. 2.4 and 2.5 are applied on the coating surface, and sliding is simulated by continuously moving the distributed tractions on the coating surface from left to right (i.e., along the positive x_1 direction in Fig. 2(c)). One complete *sliding cycle* is therefore simulated by moving the shear and normal tractions along the whole surface of the unit cell, i.e. a distance l.

3. Predicted Deformation Behaviour due to Sliding Contact

Figure 3(a) shows the deformed unit cell mesh after 100 sliding cycles calculated with the model parameters given by Eqs. 2.14 and 2.15. Note that material elements at the same distance from the contacting surface experience the same deformation histories due to the prescribed traction and boundary conditions. A narrow localised deformation region just beneath the contact surface may be seen in Fig. 3(a). In Fig. 3(b), the normalised displacement along the sliding (i.e. x_1) direction, u_1/l, is plotted against the normalised distance from the coating surface, d/l, at different numbers of sliding cycles, namely $N = 50$, 80 and 100. These results reveal that the displacement u_1 continuously increases with N within the $d/l < 0.2$ region. Beyond this region, u_1 remains almost unchanged throughout the loading history.

The predicted variation of the plastic shear strain component, ε^p_{12}, normalised by the yield strain, ε_y, is shown in Fig. 4 as a function of the normalised distance from the surface, d/l, at $N = 50$, 80 and 100. During the loading history, most of the plastic deformation occurs in the coating subsurface within the $d/l < 0.3$ region. This is well within the coating, whose thickness is $h = 0.42\, l$. From these results it can be concluded that plastic deformation in the substrate is negligible. It is also important to notice that the largest value of the shear component of plastic strain, viz. ε^p_{12}, always occurs at the same distance from the coating surface throughout the deformation history, i.e. labelled as the distance b in Fig. 4. In the present case, $b/l \approx 0.1$. Beyond this distance, the magnitude of the plastic strain in the coating decreases significantly. Note that, in general, ε^p_{ij} is the time integral

$$\varepsilon^p_{ij} \quad = \quad \int_0^t \dot{\varepsilon}^p_{ij}(\zeta)\; d\zeta \quad , \tag{3.1}$$

where $\dot{\varepsilon}^p_{ij}$ represents the (i,j) component of the corrotational plastic strain rate, which can be approximated by $\mathbf{D}^p$.

Under plane strain conditions, the plastic shear strain components ε^p_{13} and ε^p_{23} are zero. Furthermore, for the cases studied here, the magnitude of the out-of-plane plastic strain component, ε^p_{33}, is also negligibly small when compared to the in-plane components and does not accumulate during the loading history. However, the magnitudes of ε^p_{12} and ε^p_{11} at a given material point increase continuously. (Note that $\varepsilon^p_{22} \approx -\varepsilon^p_{11}$.) The variations of the plastic strain components ε^p_{11} and

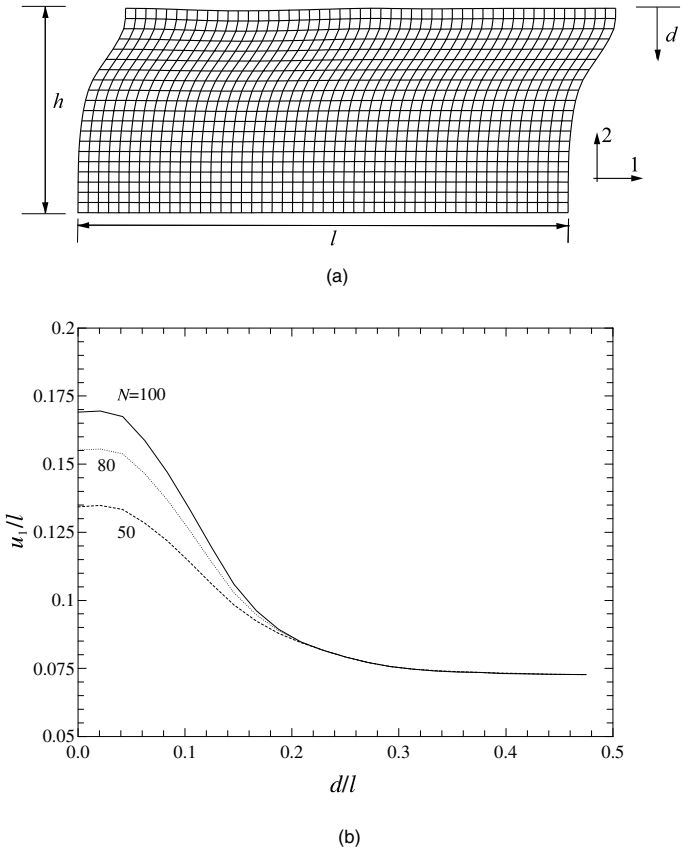

Figure 3. Deformation of the coating: (a) deformed coating mesh, to scale, shown after 100 sliding cycles; (b) variation of the tangential displacement along the depth direction at different sliding cycles normalised by the length of the unit cell model, l

ε_{12}^p during the deformation history associated with the sliding cycles, are shown in Fig. 5. Here, the strains are those at the location b, which exhibits the largest amount of plastic deformation. It may be seen that both the normal and shear strain components accumulate continuously throughout the loading history. The increase in normal strain is predicted to be considerably smaller than that of the shear strain, as shown in Fig. 5. Here the ratchetting strain will be defined as the increase in strain per loading cycle, denoted as $\delta\varepsilon_{11}^p$ and $\delta\varepsilon_{12}^p$ for the normal and shear strain components, respectively, in Fig. 5. The results show that these quantities remain almost constant after the first $\sim$ 10 sliding cycles.

Figure 6 shows the predicted cyclic variation of the plastic strain component ε_{11}^p along the sliding direction versus its counterpart stress component, T_{11}, at the depth b from the coating surface. It can be seen that, during the first few cycles, relatively large normal strains develop and that a steady state is quickly attained. In the steady ratchetting state, the magnitude of T_{11} remains almost constant from one loading cycle to the next while ε_{11}^p continuously increases with the number of sliding cycles. Since ratchetting occurs at the subsurface of the coating, the wear

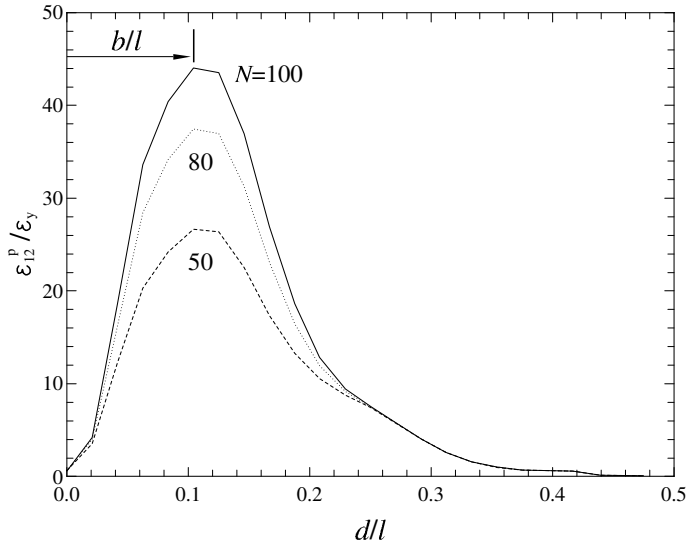

Figure 4. Variation of the plastic strain component, ε_{12}^p , normalised by the yield strain ε_y , as a function of the normalised distance from the coating surface, at different sliding cycles, N

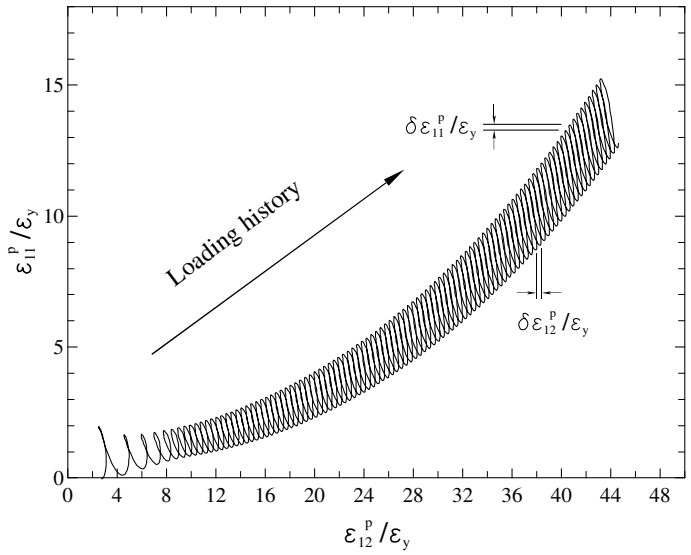

Figure 5. Accumulation of plastic strains at the depth b (see Fig. 4) during the ratchetting state

rate can therefore be obtained assuming a ratchetting-controlled failure mechanism, as outlined below.

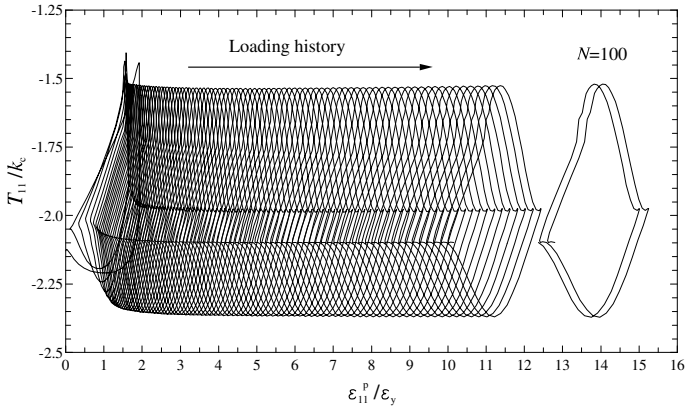

Figure 6. Variation of T_{11} vs. ε_{11}^p at depth b (see Fig. 4) during cyclic sliding

4. Wear Model Formulation

As described in Section 3, ratchetting occurs in the coating subsurface as a result of the cyclic deformation induced by successive sliding cycles, and the largest plastic shear strain develops at a fixed distance b from the coating surface. In sliding wear, the microcracks which are understood to lead to delamination wear and the subsequent formation of wear debris are driven by a combination of in-plane shear and normal plastic deformation (i.e. mixed mode I and II). The plastic shear strain component ε_{12}^p should therefore make a significant contribution to the process of initiation and propagation of delamination wear cracks. It is expected that the nucleation of microcracks due to ductile processes leading to wear failure will most likely occur at the depth b. Eventually, the layer of material from the surface down to the depth b will be removed as wear debris. Thus, the volume per unit width of the coating material removed in one periodic cell of length l by sliding wear is,

$$W = b\, l. \tag{4.1}$$

If the number of sliding cycles to failure is defined as N_f, then the corresponding total sliding distance is given by $S_{_L} = N_f\, l$. The wear rate, defined as the volume of material removed per unit width and sliding distance, can then be calculated from,

$$W' = \frac{W}{S_{_L}} = \frac{b}{N_f}\,. \tag{4.2}$$

From the multiscale mechanistic framework postulated here, the functional dependency of the critical depth b in Eq. 4.2 on the model independent parameters is,

$$b = \hat{b}_1\,\{R, l, h, p, \mu,\ \text{material properties}\}\ , \tag{4.3}$$

and, in dimensionless form,

$$\frac{b}{l} = \hat{b}_2\left\{\frac{R}{l}, \frac{h}{l}, \frac{p}{k_c}, \mu,\ \text{material properties}\right\}\ . \tag{4.4}$$

A discussion of the relative effect of each of the above independent model parameters on b and the wear rate will be given in the next section.

As discussed in Section 1, a ratchetting failure mechanism refers to a failure event which occurs when a representative plastic strain measure, which accumulates due to ratchetting, is large enough to have exhausted the local ductility of the material. It should be noted that the latter may depend strongly on the local stress triaxiality arising from geometric constraint and loading considerations. This is a similar phenomenon to ductile failure by void nucleation and coalescence, except that it takes place in a region of highly localised deformation. The number of sliding cycles to failure due to ratchetting, N_f, is therefore defined as,

$$N_f \;=\; \frac{\varepsilon_f}{\delta\varepsilon_e}\,, \tag{4.5}$$

where $\delta\varepsilon_e$ is a ratchetting strain measure per cycle and ε_f is the stress triaxiality-dependent material ductility. The ratchetting strain, $\delta\varepsilon_e$, will have a similar functional dependence on the problem parameters as b/l, Eq. 4.4.

From Eqs. 4.2 and 4.5, the wear rate relation is then given as,

$$W' \;=\; \frac{\delta\varepsilon_e\; b}{\varepsilon_f}. \tag{4.6}$$

In order to apply Eq. 4.6, the ratchetting strain $\delta\varepsilon_e$ must first be obtained. Let $\delta\varepsilon_e$ be given by the increase in the effective plastic strain between cycles in the steady state wear regime. Under uniaxial loading conditions, or if ratchetting occurs only in one direction, $\delta\varepsilon_e$ is equal to the only non-zero increase in strain component per loading cycle. In cases where multiaxial loading conditions exist, as in the problem addressed here, both ε^p_{12} and ε^p_{11} accumulate during cyclic sliding. In such cases, $\delta\varepsilon_e$ should therefore be defined as an effective strain. Following the analogy with multiaxial fatigue (e.g., Suresh, 1998), an effective plastic strain can be defined in terms of the individual components of plastic strains, ε^p_{ij}, as follows,

$$\varepsilon_e \;=\; \sqrt{\frac{2}{3}\varepsilon^p_{ij}\cdot\varepsilon^p_{ij}} \;\approx\; \sqrt{\frac{4}{3}\left[\left(\varepsilon^p_{11}\right)^2+\left(\varepsilon^p_{12}\right)^2\right]}, \tag{4.7}$$

where use was made of the relation $\varepsilon^p_{22}\approx-\varepsilon^p_{11}$ and sum is implied for $(i,j=1,3)$. It is worth pointing out that the locations which develop the maximum values of ε_e and ε^p_{12} are almost identical in the cases studied here. Both the incremental value of $\delta\varepsilon_e$ and the critical depth b can be calculated from unit cell finite element analyses and the measure of the material ductility, viz. $\varepsilon_f=\hat{\varepsilon}_f\{\sigma_m\}$, where $\sigma_m =$ trace$\{\mathbf{T}\}/3$, determined experimentally.

5. Results of Wear Analyses

(*a*) *Comparison with experimental data*

Before analysing the particular problem of interest in this work, the sliding wear model discussed in the previous section will first be used to predict the trend exhibited by typical experimental wear rate vs. contact pressure data. Gologan and Eyre (1974) measured the wear rate of a chromium flat pin rubbing against a

phosphorus bronze alloy in a pin-on-disc test over a range of applied loads. In their experiments, the pin head had a flat 30 mm^2 contacting area. In order to use the proposed micromechanics approach to predict the wear rate data, the pin-on-disc test was approximated by an equivalent plane strain wear problem for an infinitely thick coating ($h/l = \infty$), with the roughness parameter for the chromium flat pin head set rather arbitrarily to $l = 0.5$ mm. The failure strain was taken as $\varepsilon_f = 1.2$ and to be independent of the local stress triaxiality as a first approximation, and the corresponding shear strength as $k_c = 202$ MPa, which are typical values for bronze (e.g. see Coffin, 1960).

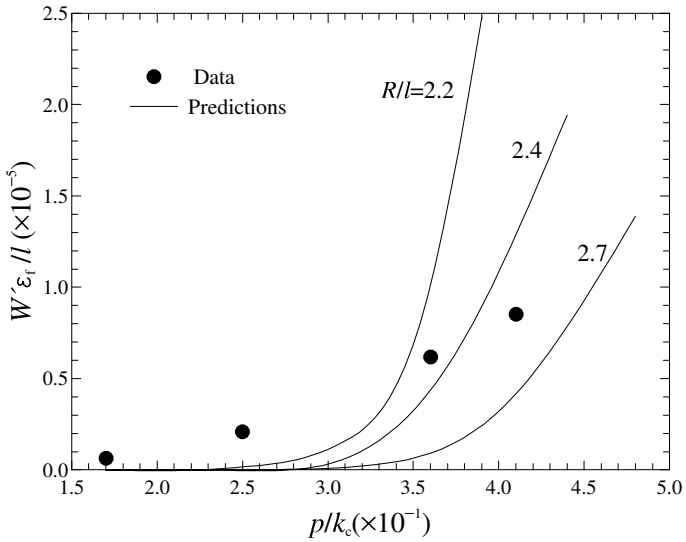

Figure 7. Comparison between experimentally measured wear rates of a phosphor bronze (Gologan and Eyre, 1974) and numerical predictions obtained with different values of R

A comparison between the wear rate data reported in the steady ratchetting state and the simulations is shown in Fig. 7. Here, the data were fitted with different values of R, labelled $R/l = 2$,2, 2.4 and 2.7. The general predicted trend and the overall magnitudes of the wear rates are consistent with the data. It is seen, however, that the assumption of a load independent asperity radius R is not fully validated by the results shown in Fig. 7, as a single value of R/l will not adequately fit all the data. However, if R increases with the applied pin-on-disc load, as one would expect for a relatively soft pin material such as Cr, then Fig. 7 predicts the data more accurately. A decrease in the value of R, for a given load, results in a higher wear rate, due to the corresponding increase in the maximum contact pressure, p_o in Eq. 2.1, and decrease in the contact half-width, a in Eq. 2.2. The effect of variations in the asperity radius could be quantified by the results of Fig. 7. However, as there were insufficient data in the work of Gologan and Eyre (1974) and no information on typical asperity radii, accurate quantification of the effect is not possible. Note that for $p/k_c < 2.5$ the predicted wear rate is negligible as the ratchetting plastic strain generated in the coating at these pressures is negligibly small.

(*b*) *Effect of model parameters on wear rate*

In this section, the effect of the most relevant model parameters on the wear rate of a coated die used in a stamping process is discussed. In all the results to be reported here, the friction coefficient is taken as $\mu = 0.1$ and $h/l = 0.42$, unless otherwise specified. Furthermore, wear rates are normalised by ε_f and l, as they are considered invariants for a given material and loading condition. As discussed in Section 3, the pressure, p (Eq. 2.15), was determined from a finite element simulation of the stamping problem at the macro-scale (Tunvisut *et al.*, 2000).

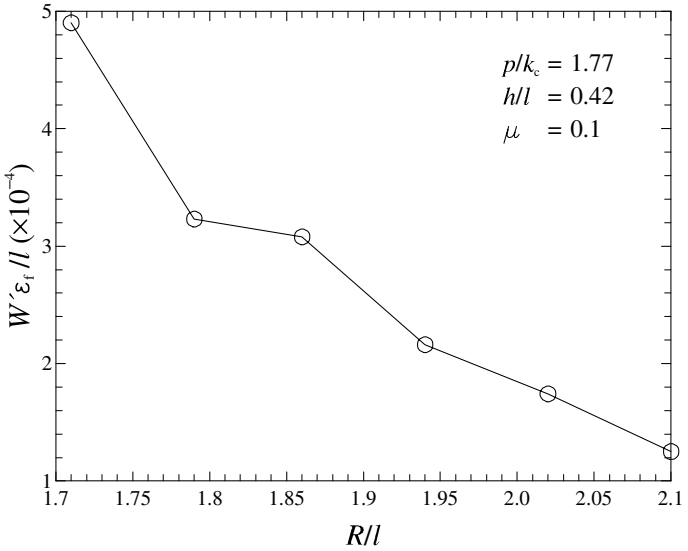

Figure 8. Effect of the asperity's initial contact radius on the predicted wear rate

The predicted dependence of the wear rate on the asperity radius R is shown in Fig. 8 for $p/k_c = 1.77$. It can be seen that the normalised wear rate decreases with increasing values of R, when the contact load and spacing between asperities, l, are kept fixed. As a rough surface is associated with low values of R, the predictions imply that a rougher contacting surface will increase the wear rate of the coating. Thus, an efficient way to prolong the life of the coating is to smooth the surface of its contacting partner. While this observation is qualitatively supported by experimental observations in a range of materials (e.g., see Akkurt, 1995), further experimental verification is needed to quantify that effect.

For a given level of surface roughness, as was seen in Fig. 7, the wear rate depends on the nominal contact pressure, p. In the stamping simulations, the normal pressure in the sliding region ranges between $1.3 \leq p/k_c \leq 1.8$ over most of the stamping history. The sensitivity of the wear rate to variations in p is investigated in Fig. 9 for $R/l = 1.79$. The strong, near linear, dependence of wear rate on pressure may be seen, suggesting that using the maximum pressure to predict wear rate will give a significantly conservative prediction.

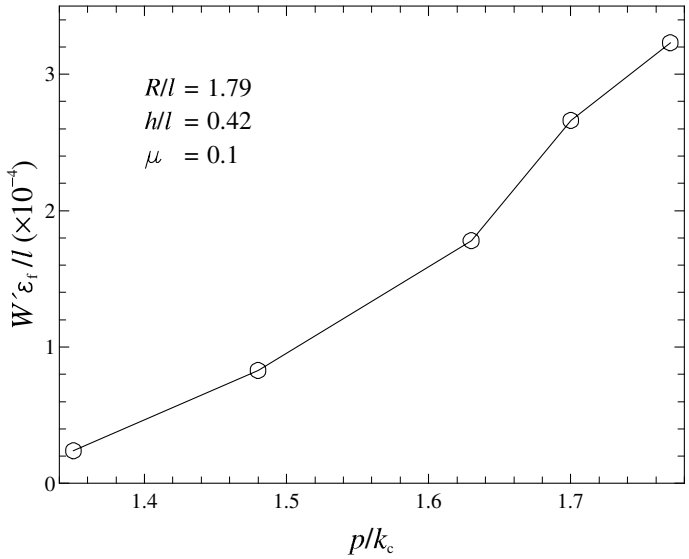

Figure 9. Effect of the average contact pressure on the predicted wear rate

The influence of the friction coefficient on the wear rate is shown in Fig. 10 for $p/k_c = 1.77$ and $R/l = 1.79$ (these values give $p_0/k_c = 4.52$ and $a/l = 0.25$). The results show the wear rate to be highly sensitive to the friction coefficient at these relatively high load levels. An increase in the friction coefficient produces higher tangential tractions and this, in turn, give rise to larger plastic strain amplitudes causing the wear rate to increase. Thus, the benefit of using lubrication or, indeed, self-lubricating coatings to improve wear resistance, may be quantified from these types of predictions.

In practical applications, the coating thickness h is an important design parameter. Thus the variations of the wear rate with h was also investigated. The results are shown in Fig. 11 by the solid line, where it can be seen that the wear rate decreases with coating thickness for $h/l < 0.5$ and then remains almost constant. A threshold thickness can therefore be identified beyond which the wear rate remains unaffected. In other words, for the load and asperity radius given in Fig. 11, the influence of the substrate on the wear rate disappears when $h \sim l/2$. The behaviour of the coated component then approaches that of an homogeneous material with the properties of the coating. However, note that an increase in the applied nominal pressure will result in an increase in b and hence give a higher threshold thickness. Figure 11 also shows that the corresponding values of the localization depth b remain practically unaffected by thickness changes, down to $h \leq 0.3\,l$.

In all the results reported so far, the coating strain hardening behaviour was assumed to be that exhibited by bulk Mo. To assess the effect of the material strain hardening behaviour on the wear rates, computations were performed for coatings with the different cyclic stress-strain curves given in Fig. 12(a). Thus the range of idealised coating materials are assumed to have a common yield stress but different kinematic hardening behaviour. For simplicity, the curves shown in Fig. 12(a) will be identified by the exponent, n, which would be required to fit the hardening

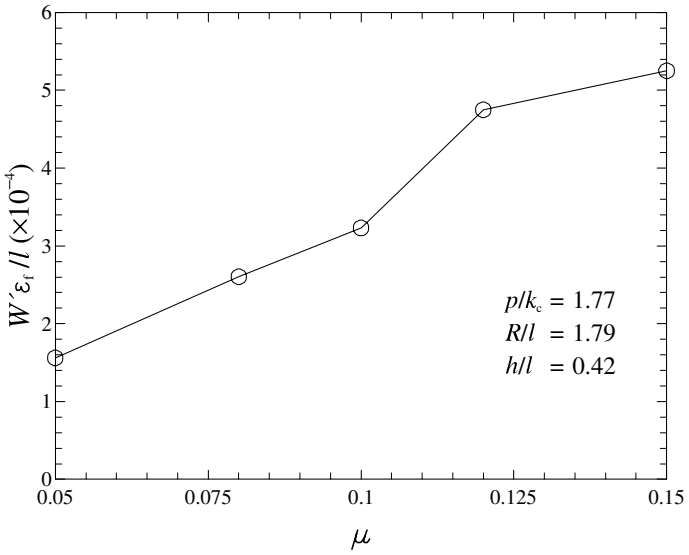

Figure 10. Effect of the friction coefficient on the predicted wear rate

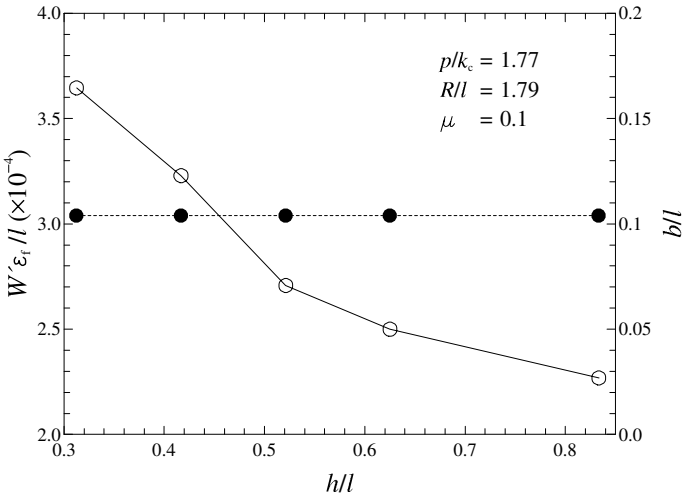

Figure 11. Effect of normalised coating thickness on the wear rate and the critical depth

behaviour of each curve monotonically using the following equivalent power law,

$$\tilde{\varepsilon} = \tilde{\varepsilon}_y \left(\frac{\tilde{\sigma}}{\sqrt{3}\, k_c} \right)^n, \qquad \text{for } \tilde{\sigma} > \sqrt{3}\, k_c, \tag{5.1}$$

where $\tilde{\sigma}$ is the equivalent uniaxial stress, and $\tilde{\varepsilon}_y$ the yield strain defined as $\tilde{\varepsilon}_y = \sqrt{3}k_c/E_c$. A direct correspondence can be found between the power law exponent n and the kinematic hardening parameters H_c and C in Eq. 2.13. For instance, a value of $n = 9$ corresponds to the values of $H_c = 3.04$ and $C = 3.6$ calibrated from bulk Mo data.

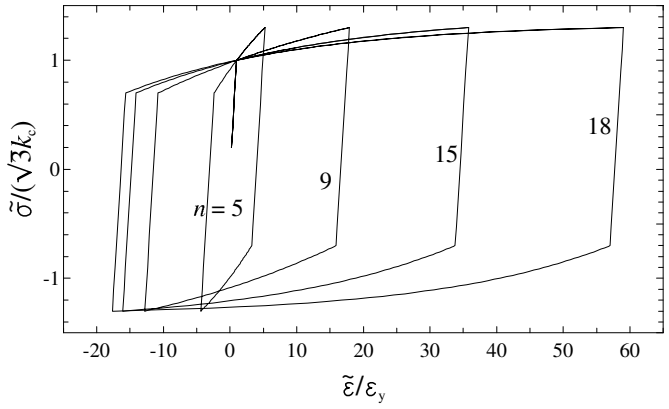

(a)

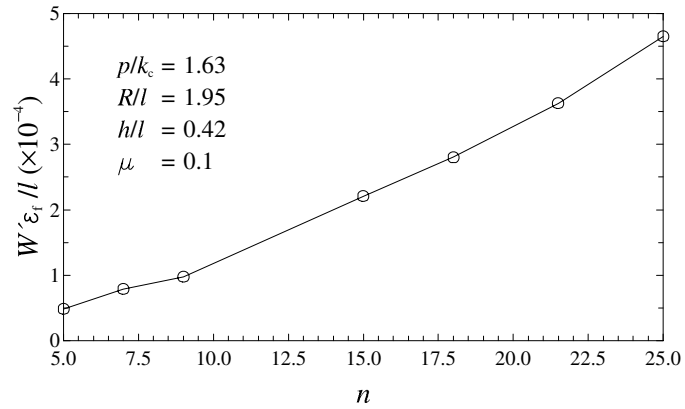

(b)

Figure 12. (a) Influence of the hardening exponent n on the coating's uniaxial stress-strain behaviour; and (b) predicted effect of the hardening exponent on the wear rate

It can be seen in Fig. 12(a) that, as n increases with a given stress level, the amount of plastic strain increases. The predicted effect of varying n on the wear rate is shown in Fig. 12(b). As expected, the wear rate increases with the hardening exponent. Thus the stronger the strain hardening behaviour of the coating material, the better wear resistance properties can be expected.

6. Discussion

In this work, the formulation of the proposed multiscale continuum mechanics approach has relied on an idealisation of the contact between a smooth and a relatively rough surface as a series of periodically arranged unit cells at the mesoscale subjected to repeated sliding contact. This requires that the roughness of the contacting surface be characterised to identify the length of the unit cell model and the characteristics of the contact pressure distributions.

In the unit cell analyses, material points at the same depth from the surface experience the same plastic deformation histories and a layer of material is removed above the position at which the largest plastic shear strain develops. The removal of one layer of material is then considered to determine the wear rate. The overall wear behaviour will however involve the removal of successive layers of material until the coating is completely worn away. The wear rate will then be different for each successive layer, as the ratio, h/l, decreases on removal of each layer. Based on the results shown in Fig. 11, it is therefore expected that the number of sliding cycles to failure will decrease for the second and successive layers. It is also possible that some amount of plastic deformation will have accumulated at the depth $\approx 2b$ from the original coating surface by the time the first layer is removed leading to a further increase in wear rate for the second and subsequent layers. However, from the steep nature of the local strain gradients at the depth b, e.g. see Fig. 4, this effect is expected to be secondary and is therefore not accounted for in this study.

The number of sliding cycles to failure for a generic layer i, N_{fi}, is given as b_i/W_i' (see Eq. 4.2), where b_i is the critical localization depth for the layer i, and W_i' the corresponding wear rate. The total number of sliding cycles to failure, N_T, will then be given by

$$N_T = \sum_{i=1}^{\text{no. layers}} \frac{b_i}{W_i'} \ . \tag{6.1}$$

The total number of sliding cycles required to wear away coatings of different thickness, as predicted by Eq. 6.1, are given in Fig. 13. Here, the normalised pressure and asperity radius have been assumed to be $p/k_c = 1.77$, and $R/l = 1.79$, respectively, and $\epsilon_f = 1.0$. It is worth noting that, for this load level, a near-linear dependence of life on h is predicted.

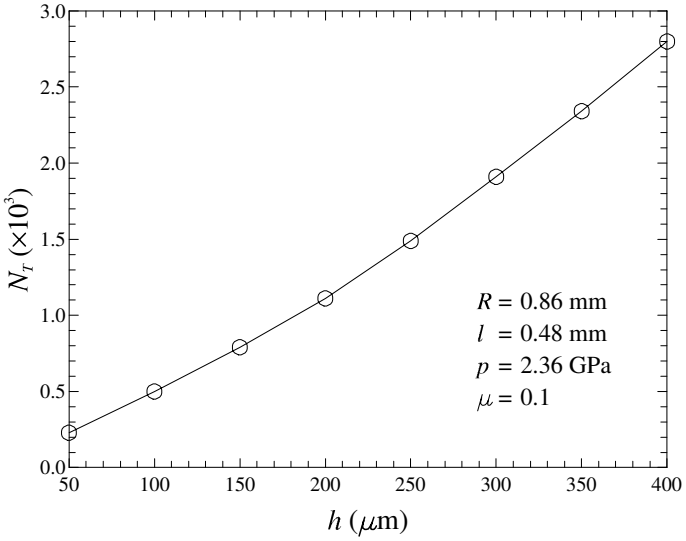

Figure 13. Estimated life of the coating as a function of the coating thickness

The sliding life given by Eq. 6.1 can be thought of as a mesoscopic measure of life. At the macroscale, however, for instance in a stamping process, a prediction of the number of *stamping* operations to failure is required. Let S be the sliding distance experienced by a point on the coating surface in one stamping operation. This quantity can be obtained directly from the same macroscopic finite element analyses conducted to extract the pressure, p. The sliding distance in one sliding cycle is the distance between asperities, l. Therefore the number of stamping operations to failure will be given by,

$$N_S = \frac{l}{S} N_T \approx \frac{l}{S} b \sum_{i=1}^{\mathrm{int}(h/b)} \frac{1}{W_i'} , \tag{6.2}$$

where use was made of the negligible effect of coating thickness on b (see Fig. 11) and the number of layers removed was approximated by the integer value of h/b. A typical value of the sliding distance calculated from the macroscopic FE analyses of the stamping process was $S = 0.4$ mm. Thus, with $l = 0.5$ mm, $h = 0.35$ mm, and the results of Fig. 13, one finds that $N_S \approx 3000$, which is a reasonable value. A parametric study using sliding distances of relevance to stamping and other similar processes together with a detailed discussion of life prediction of coated components will be given in Tunvisut *et al.* (2000).

In the proposed multi-scale approach, a modified Hertzian contact theory has been used to represent the contact pressure distributions which would be obtained when the effects of plastic deformation are accounted for. Here, a parameter λ in Eqs. 2.1 and 2.2 is used to scale the magnitudes of p_0 and a given by the Hertzian relations. Further work is required to calibrate λ for a wider range of roughness characteristics (i.e., R and l) and coating properties from reference pressure distributions obtained from elastic-plastic finite element contact simulations. Furthermore, in the current work, the surface tractions are assumed to remain unchanged during the cyclic sliding history. In practice, they may vary due to changes in either the contact geometry or the magnitude of the nominal applied contact pressure, p. If the loading history and/or any changes in the friction coefficient, μ can be determined, then values of b and ε_e numerically predicted with the proposed unit cell approach can be used, in conjunction with Eq. 4.6, to predict the wear behaviour of the coating under such conditions.

It should also be noted that the depth beneath the surface at which the maximum shear deformation is found is predicted to decrease with increasing friction. It is therefore expected that the critical depth b will become negligibly small for contacting surfaces with very high friction coefficients (e.g., $\mu \gg 0.2$). In such cases, microcracks would likely originate from the coating surface, and a different approach would be required to determine the volume of material removed.

In our calculations, the coating material is assumed to be homogeneous. However, some coating deposition methods are known to leave inhomogeneities within the material, such as porosities during plasma-spraying. Furthermore, the coating may also be composed of two or more metallic phases, e.g. Mo + AlSi, with contrasting properties. It has also been experimentally observed that microstructures such as dislocation cells develop at heavily deformed fragmented layers during sliding contact (Rigney and Glaeser, 1978). The appearance and/or subsequent development of such microstructural inhomogeneities during service will affect the local

material properties and hence the wear behaviour. For a particular material, the local microstructural evolution during deformation and its effect on the local material flow stress can be accurately described through the use of physically based internal variable constitutive formulations (e.g., see Busso, 1998). Alternatively, inhomogeneities at the mesoscale (e.g. phase constitution, porosities) can be introduced explicitly into the unit cell FE model. This is however outside the scope of this work and will be addressed in future work.

7. Summary

A multiscale mechanistic approach has been developed to study the effect of surface and microstructural parameters and local contact conditions on the rate of sliding wear during a metal working process. Contact between a relatively rough body and a smooth coating at the mesoscale has been considered. The mechanical response of the coating due to repeated sliding contact has been obtained from finite element analyses of a representative unit cell model. A ratchetting wear model, assumed to be controlled by the accumulation of plastic deformation in the coating subsurface, has been formulated and used to conduct a parametric investigation into the effect of material, loading, surface roughness and geometrical parameters on the wear rate. An expression is also given to link the maximum number of sliding cycles at the level of each individual asperity, or mesoscale, with the macroscopic maximum number of stamping operations required to wear away the coating. The predictions show that the wear rate increases with contact pressure and depends strongly on the coating thickness and the roughness of the counterpart surface. It is also found that a reduction in the friction coefficient and an increase in the coating strain hardening behaviour can considerably improve the wear resistance of coated components. The predicted trends are generally consistent with experimental observations; however, some of them need to be experimentally verified in future work. The proposed framework can also be applied to investigate the sliding wear behaviour of uncoated components.

Acknowledgements

This work has been supported by the European Union through the BE Project 97-4283, COMPWERC. ABAQUS was provided under academic license by HKS Inc., Providence, Rhode Island, USA.

References

ABAQUS V. 5.8, 1998. Hibbitt, Karlsson and Sorensen Inc., Providence, RI.

Akkurt, S., 1995. On the effect of surface and roughness on wear of acetal-metal gear pairs. *Wear* **184**, 107-109.

Busso, E.P., 1998. A continuum theory for dynamic recrystallization with microstructure-related length scales. *Int. Journal of Plasticity*, **14**, N. 4-5, 355-372.

Challen, J.M. & Oxley, P.L.B., Hockenhull, B.S. 1986. Prediction of Archard's wear coefficient. *Wear* **111**, 275-288.

Coffin, L.F. 1960. The stablility of metals under cyclic plastic strain. *Trans. ASME J. Basic Engng* **82D**, 671-682.

COMPWERC 1998, Brite EuRam project, BE97-4283.

Dautzenberg, J.H. & Zaat, J.H. 1973. Quantitative determination of deformation by sliding wear. *Wear* **23**, 9-19.

Gologan, V. & Eyre, T.S. 1974. Friction and wear of some engineering materials aganist hard chromium plating. *Wear* **28**, 49-57.

Habig, K. -H. 1989. Wear behaviour of surface coatings on steels. *Tribology International*, **22**, 65-73.

Haferkamp, H., Gerken, J., Toenshoff, H.K. & Marquering, M. 1996. Laser alloying of molybdenum on steel surfaces to increase wear resistance. In *Proceedings of the 1995 9th International Conference on Surface Modification Technologies* (ed. T.S. Sudarshan, W. Reitz & J.J. Stiglich), pp. 547-564. Warrendale: The Minerals, Metals & Mats. Soc.

Jahanmir, S. & Suh, N.P. 1977. Surface topography and integrity effects on sliding wear. *Wear* **44**, 87-99.

Johnson, K.L. 1985. Contact mechanics. Cambridge: Cambridge University Press.

Kapoor, A. 1994. A Re-evaluation of the life to rupture of ductile metals by cyclic plastic strain. *Fatigue Fract. Engng Mater. Struct.* **17**, 201-219.

Kapoor, A. & Johnson, K.L. 1994. Plastic ratchetting as a mechanism of metallic wear. *Proc. R. Soc. Lond. A* **445**, 367-381.

Kapoor, A., Johnson, K.L. & Williams, J.A. 1996. A model for the mild ratchetting wear of metals. *Wear* **200**, 38-44.

Monaghan, D.P., Laing, K.C., Logan, P.A. & Teer, D.G. 1993. Advanced hard and soft coatings for high performance machining and forming. *Finishing* **17**, 6p.

Rigney, D.A., Divakar, R. & Kuo, S.M. 1992. Deformation substructures associated with very large plastic strains. *Scripta Met. Et. Mat.* **27**, 975-980.

Rigney, D.A. and Glaeser, W.A., 1978. The significance of near surface microstructure in the wear process. *Wear*, **46**, 241-250.

Ruff, A.W. 1976. Deformation studies at sliding wear tracks in iron. *Wear* **40**, 59-74.

Suh, N.P. 1980. Update on the delamination theory of wear. In *Sliding wear mechanisms, in Fundamentals of friction and wear of materials* (ed. D.A. Rigney), pp. 43-70. Metals Park: American Society for Metals.

Suresh, S. 1998. Fatigue of materials. 2nd ed. Cambridge University Press, Cambridge.

Tunvisut, K., O'Dowd, N. P., and Busso, E. P. 1999. Use of scaling functions to determine mechanical properties of thin coatings from microindentation tests. To be published in the *Int. J. Solids and Structures.*

Tunvisut, K., O'Dowd, N. P., and Busso, E. P. 2000. Computational Studies of Contact in Coated Stamping Tools. Manuscript in preparation.

Wayne, S.F., Sampath, S. & Anand, V. 1994. Wear mechanisms in thermally-sprayed Mo-based coatings. *Tribology Transactions* **37**, 636-640.

Yan, W., and Fischer, F. D. 1999. Verifying the application of Hertz contact theory to rail-wheel contact problems. To appear in the *Archive of Applied Mechanics.*

Ziegler, H. 1959. A modification of Prager's hardening rule. *Quart. Appl. Math.*, **17**, 55-65.